Electrochemistry Communications 132 (2021) 107134

Contents lists available at ScienceDirect

Electrochemistry Communications

journal homepage: www.elsevier.com/locate/elecom

Fracture-induced aging anomalies in $LiNi_{0.6}Mn_{0.2}Co_{0.2}O_2$ electrodes

Saeed Yari [a,b], Jan D'Haen [a,c], Marlies K. Van Bael [a,b,c], An Hardy [a,b,c], Mohammadhosein Safari [a,b,c,*]

[a] Institute for Materials Research (IMO-imomec), UHasselt, Martelarenlaan 42, B-3500 Hasselt, Belgium
[b] Energyville, Thor Park 8320, B-3600 Genk, Belgium
[c] IMEC Division IMOMEC, BE-3590, Belgium

ARTICLE INFO

Keywords:
Porous electrode
Aging
Lithium redistribution
Fracture

ABSTRACT

The gradual loss of capacity and increase in the cell impedance are the mainstream of aging patterns for the lithium-ion batteries and mainly result from the depletion of cell's cyclable-lithium reservoir. The irreversible drain from this reservoir is well understood and originates from the phenomena such as electrolyte oxidation and reduction at the electrode/electrolyte interfaces. There is, however, limited knowledge about the circumstances leading to the recuperation of misplaced lithium, gain in cell's energy, and impedance drop. Here, we showcase that the intragranular fracture induces a peculiar aging behavior in the $LiNi_{0.6}Mn_{0.2}Co_{0.2}O_2$ electrodes. Fracture enables an alternative path for the (de)insertion of lithium from the hard-to-reach center of the secondary particles by lithium pore-wall flux instead of solid-state diffusion. The possible consequences are the energy recovery and decrease of the charge-transfer resistance in the electronically well wired electrodes.

1. Introduction

Porous electrodes with high areal loadings of densely packed active-material particles are very desired for the development of high energy density lithium-ion and lithium batteries. Increasing the thickness of the porous electrodes and use of polycrystalline active materials packed from primary particles are popular strategies in the research and development of cathodes such as $Li[Ni_{1-x-y}Co_xMn_y]O_2$ (NMC) [1–3]. These strategies, however, render the electrodes more vulnerable to the structural inhomogeneity and limit their operation to lower C-rates to avoid premature end of life [4–7]. At the electrode level, the most common forms of heterogeneity in the porous electrodes are process induced and reported to be the spatial variance in the electrode composition [8,9], carbon-binder morphology [10–12], particle size [4,13], tortuosity [14,15], and contact resistances [16]. At particle scale, the anisotropic lattice breathing of the NMC primary particles induces inter- and intra-granular fracture in the secondary NMC particles [17–19]. Upon delithiation the Young's moduli, interfacial fracture toughness and the cohesive energy of the NMC materials decrease and the volume change of primary particle causes cracks to form at the interfaces and grain boundaries where the diffusion induced stress exceeds the cohesive strength [20,21]. Such circumstances, notwithstanding the length scale, entail the fragmentation of the total active mass into the under-utilized zones versus over-utilized or hotspots within the porous electrode. As such the local lithiation state of the active material particles can be significantly different from the bulk average values at high current densities [22,23]. For instance, if the transport limitations within the electrolyte exceed that of the porous electrode solid phase then the active particles located next to the separator are overstressed during (dis)charge [24,25].

Here, we analyze the dynamics of aging during 200 cycles for a series of porous $LiNi_{0.6}Mn_{0.2}Co_{0.2}O_2$ electrodes from the perspective of cyclable lithium (re)distribution in a cell with $Li_4Ti_5O_{12}$ (LTO) as anode active material. We use different configurations of electronic percolation network in the four otherwise analogous porous electrodes formulated with 94%wt polycrystalline NMC particles and 2.5%wt carbon. This model experimental system highlights the sensitivity of the cell aging trajectory to the synergistic interaction of the electrode's microstructural detail and the intragranular fracture of secondary NMC particles [26]. The choice of LTO counter electrode and a voltage window of 1.4–2.8 V was made to limit the kinetics of electrolyte reduction and oxidation at the anode and cathode interfaces with the electrolyte and that of irreversible transformation of NMC from layered to the spinel or rock-salt structure. Such a framework, unlike the existing literature [27–30], facilitates it to correlate the evolution of cell metrics (i.e. capacity and impedance) with the dynamics of lithium redistribution

* Corresponding author.
E-mail address: momo.safari@uhasselt.be (M. Safari).

https://doi.org/10.1016/j.elecom.2021.107134
Received 4 September 2021; Received in revised form 26 September 2021; Accepted 29 September 2021
Available online 3 October 2021
1388-2481/© 2021 The Authors. Published by Elsevier B.V. This is an open access article under the CC BY-NC-ND license (http://creativecommons.org/licenses/by-nc-nd/4.0/).

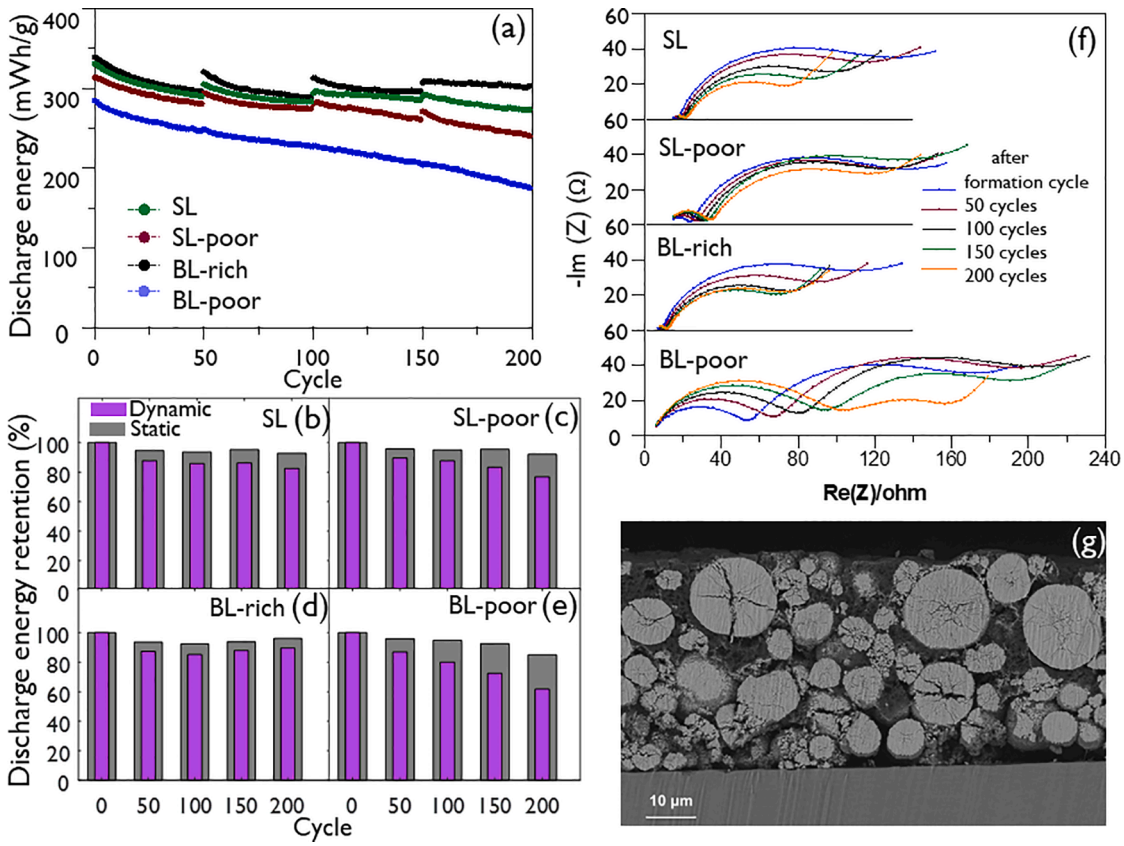

Fig. 1. a) Discharge energy of LTO|NMC cells as a function of cycle number, b-e) discharge energy retention after every 50 cycles during duty cycles at 1C (dynamic) and after intermittent C/10 titration (static) f) Nyquist plots of the cell impedance spectra recorded after every 50 cycles during the intermittent characterization periods g) cross section SEM micrograph of the BL-poor electrode after 200 cycles.

among 'cyclable,' and 'inactive' states. We demonstrate that the fracture at NMC grain boundaries has two main effects on the lithium balance inside the cell. Beyond promoting the permanent loss of lithium (inactivation) via the interfacial side reactions at fresh interfaces, intragranular fracture can improve the uniformity of lithium distribution by exposing hard-to-reach interior of the secondary NMC particles to the electrolyte for the direct pore-wall flux of lithium.

2. Materials and methods

2.1. Model experimental system for NMC electrodes

A single layer NMC electrode with a porosity of 30%, hereafter referred to as SL, represents a conventional design and serves as a reference in this study. Two distinct methods were used to prepare 3 other electrodes with different electronic conduction path with respect to the reference design (SL). In the first method, a low level of calendaring was used to densify one single-layer electrode to a final porosity of 40%, hereafter referred to as SL-poor, compared to the 3 other electrodes with porosity of 30%. In the second approach, two bilayer electrodes were prepared by an uneven allocation of the carbon (2.5%) between the two layers [8]. As such, BL-poor and BL-rich bilayer electrodes are featured with a carbon deficient (1%) and carbon rich (4%) layer close to the current collector, respectively (see supporting information).

2.2. Characterization

Electrochemical cycling of the Li|NMC and LTO|NMC 2025 coin cells was done with a Biologic BCS-805 battery cycler. The coin cells were assembled in an M−Braun glovebox (H_2O & $O_2 < 1$ ppm), with Celgard 2325 as the separator and EC: EMC 3:7, 1 M $LiPF_6$ + 2 wt% VC as electrolyte. The cells were allowed to rest for 24 h before formation cycles: three charge and discharge cycles at C/10 in the potential window of 1.4–2.8 V. The formation cycle ended with 1 h of rest and eventually the galvanostatic aging cycling of the cells initiated with symmetric (dis)charge at 1C for 200 cycles. To follow the state-of-health of the cells during the aging cycling tests, an intermediate characterization period was foreseen after every 50 cycles. These intermediate tests consisted of a low rate (dis)charge cycle at C/10 and the electrochemical impedance spectroscopy (EIS) in a frequency range of 10 kHz-10 mHz with a voltage amplitude of 5 mV. At the end of aging tests, the cells were opened in the glovebox and electrode punches were rinsed with DMC solvent for 30 sec to remove the remnants of the electrolyte, and dried overnight in the glovebox environment for further postmortem analyses. The cross-section of the cathode punches was prepared by ion beam polisher and imaged with Zeiss 450 FEG-SEM with Gemini 2 optics. Details of differential capacity analysis used for the estimation of stoichiometry window of NMC electrodes during cycling and the equivalent-circuit modelling of EIS spectra are discussed in the supplementary information.

3. Results and discussion

Fig. 1a summarizes the cycling performance of the four LTO| NMC cells assembled with the SL, SL-poor, BL-poor, and BL-rich cathodes during 200 (dis)charge cycles at 1C. The BL-rich cell has the highest initial discharge energy (339.5 mWh/g) together with a discharge capacity of 151.5 mAh/g, and an average discharge voltage of 2.241 V (see Table S1 and Fig. S1 in Supporting information). SL cell shows the second best performance (331.3 mWh/g) followed by the SL-poor (313.7 mWh/g) and the BL-poor (284.7 mWh/g). The remaining

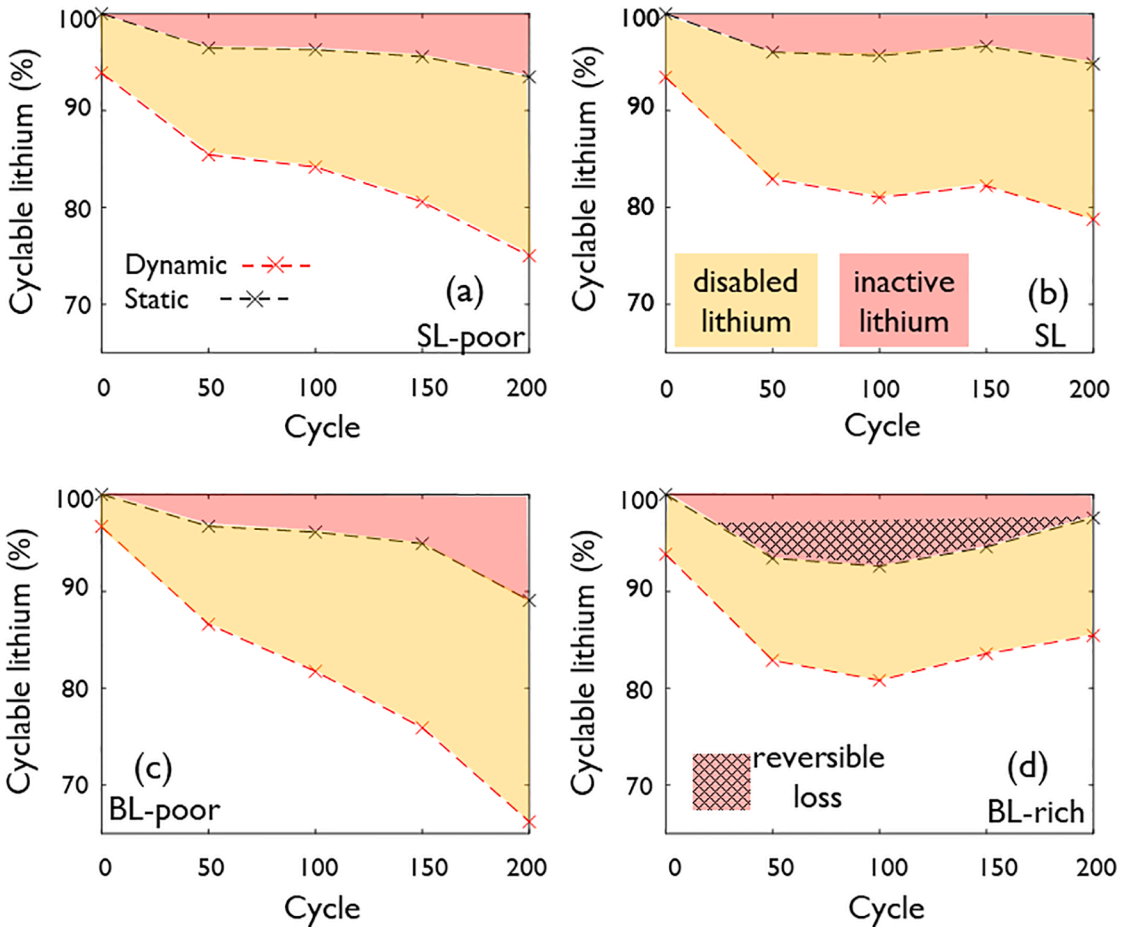

Fig. 2. Fractional variations in the amount of cyclable lithium in the LTO|NMC cells during 200 cycles obtained from the analysis of 1C duty discharge (dynamic, red markers) and C/10 discharge data during intermittent characterization periods (static, black markers). Cells differ in the NMC electrode: a) SL-poor, b) SL, c) BL-poor, d) BL-rich. (For interpretation of the references to color in this figure legend, the reader is referred to the web version of this article.)

discharge energy of the cells after 200 cycles and according to the duty cycles at 1C (dynamic) reads 89.5%, 85.5%, 76.76 %, and 61.72% for the BL-rich, SL, SL-poor and BL-poor cells, respectively. Noteworthy is the continuous increase in the performance deviation among the four cells during the cycling. The coefficient of variance for the discharge energy of the cells grow from 7.5% at the beginning of life to 21.8% after 200 cycles. Fig. 1b-e highlights the higher energy retention relative to the dynamic values for all the cells measured at C/10 during the intermittent characterization periods (static) every 50 cycles. The BL-rich cell manifests a counterintuitive energy recovery (Fig. 1d). In this cell, the energy loss during the first 100 cycles is later recovered by 50% and 29% in the static and dynamic conditions, respectively. The impedance evolution reveals another peculiar behavior which is the reduction of charge transfer resistance over some periods of cycling in all the cells (Fig. 1f) [31]. The prima facie explanation for these observations is the tendency of secondary NMC particles to fracture which is observed in our electrodes (Fig. 1g).

The lithium stoichiometry window ($\Delta x = x_{max} - x_{min}$) in the Li_x-$Ni_{0.6}Mn_{0.2}Co_{0.2}O_2$ electrodes were tracked by analysing the differential capacity signature of the cells over 200 cycles (Figure S2-4). All the electrodes reach a fully lithiated state ($x_{max} = 1$) during the static conditions (C/10) irrespective of the cycle number. There is, however, a clear sign of sever cycling impact on the degree of lithium deinsertion (x_{min}) from the NMC under both static and dynamic conditions (Figure S4). The variation in x_{min} as a function of cycle number is more pronounced in the dynamic ($0.42 < x_{min} < 0.61$) compared to the static ($0.37 < x_{min} < 0.44$) conditions. The change in Δx is an ideal gauge to follow the evolution in the amount of cyclable lithium inside the LTO|NMC cells (Fig. 2). Overall, there is less and less lithium taking part in the (dis)charge of the four cells over 200 cycles. The gradual change in the percentage of cyclable lithium is much higher for the dynamic (red dashed lines in Fig. 2) relative to the static (black dashed lines in Fig. 2) tests due to the larger polarization at higher currents (1C). As such the cyclable-lithium deviation between the static and dynamic conditions (brown highlighted area in Fig. 2) represent the fraction of lithium disabled on account of the gradual rise in the cell impedance. The BL-rich cell manifests an unusual recovery in cyclable lithium (Fig. 2d) which is at clear contrast to the other three cells with a rather monotonic declining trend for cyclable lithium (Fig. 2a-c). This observation is in line with the energy recovery of the BL-rich cell mentioned earlier (Fig. 1d). The so called irreversible loss of cyclable lithium into the parasitic reaction products is traditionally inferred from the low rate titration data during the static tests (red dashed area in Fig. 2d) [32]. However, the clear sign of lithium recovery in the BL-rich cell (fence patterned area in Fig. 2d) calls for a reactivation mechanism in the NMC electrodes.

In the absence of cracks in the secondary NMC particles, the (de) insertion of lithium from the central domains (central rectangles in Fig. 3a-d) is kinetically hindered mainly by the solid-state lithium diffusion. These parts experience a relatively higher polarization and end up with a higher average lithium residue (x) and a sharper lithium concentration gradient by the end of charge. The intragranular fracture (Fig. 3e and S6) exposes the interior of the secondary particles to the liquid electrolyte [33]. Therefore, the active electrode area in direct contact with the electrolyte increases resulting in two major consequences. First, the electrolyte decomposition and interfacial side

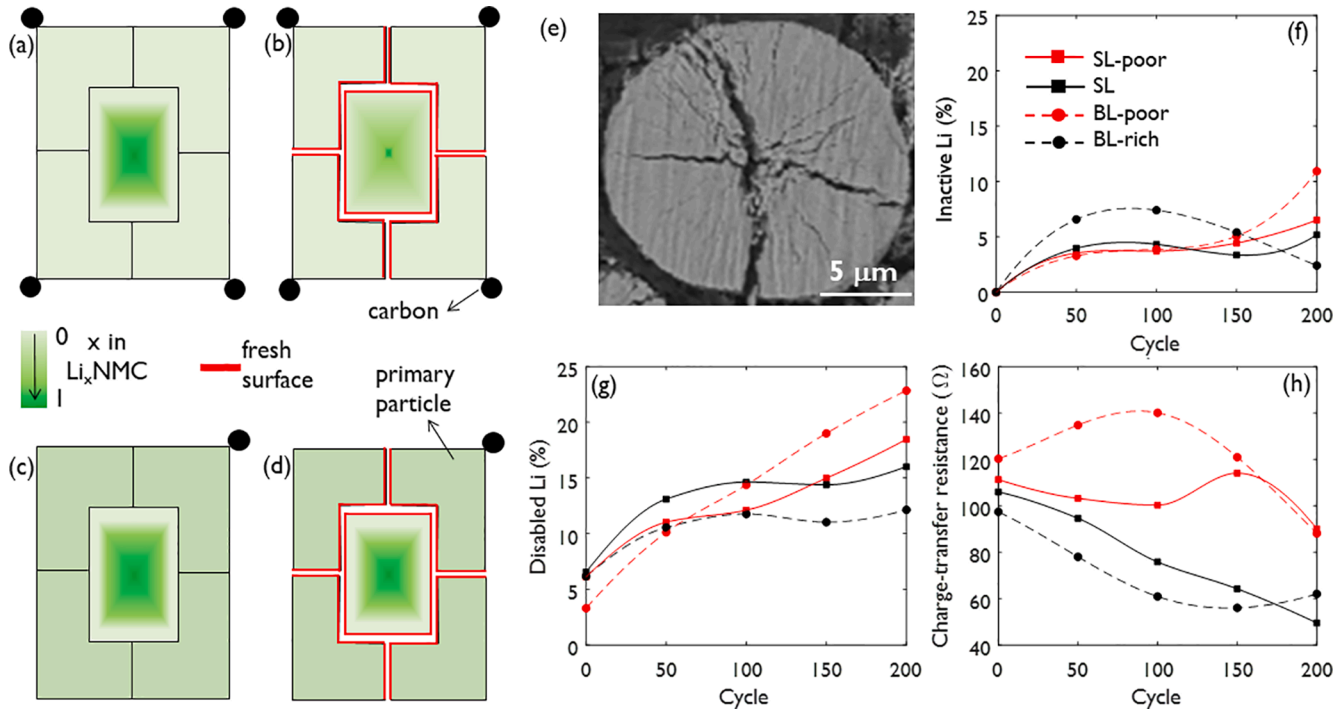

Fig. 3. Schematic representation of lithium distribution color coded in shades of green a,c) before and b,d) after e) intragranular particle fracture and exposure of new surfaces (red edges) to the electrolyte in the NMC electrodes with a,b) optimal electronic percolation and c,d) poor conduction networks. Variations in f) inactive lithium, g) disabled lithium, and h) charge transfer resistance for the LTO|NMC cells with SL, SL-poor, BL-poor, and BL-rich cathodes over 200 cycles. (For interpretation of the references to color in this figure legend, the reader is referred to the web version of this article.)

reactions at the fresh interfaces are promoted in favour of lithium loss and the growth of cathode electrolyte interphase, i.e. CEI (red boundaries in Fig. 3b, d). Second, the (de)insertion of lithium from the otherwise hard-to-reach centre of the secondary particles is facilitated due to the possibility of direct lithium exchange at particle/electrolyte interface (pore-wall flux). This can be interpreted as a lithium recovery mechanism leading to a more spatial uniformity of lithium (Fig. 3a-d) and a higher degree of lithium deinsertion from the NMC electrode as evidenced by the gradual decline of x_{min} in the BL-rich electrode after 100 cycles (Figure S4).

After formation cycles, the fraction of inactivated lithium, with respect to the beginning of life, in the LTO|NMC cells (Fig. 3f) is mainly determined from the counterbalance between the lithium loss for the formation of cathode electrolyte interphase (CEI) and recovery mechanisms triggered by the fracture at the grain boundaries. The configuration of the carbon matrix has a crucial impact on the dynamics of lithium deactivation in the NMC electrodes. The lithium recovery is insignificant for the poorly carbon-wired secondary particles (Fig. 3c-d) on account of the high probability for aggravation of electronic limitations for the internal particles after fracture. The consequence is a non-uniform current distribution and creation of the hot spots where the local polarization is higher and therefore the electrolyte degradation and crack growth are accelerated. Such a degradation runaway is evidenced in the SL-poor and BL-poor electrodes by the continuous rise in the percentage of inactive lithium during 200 cycles (Fig. 3f). In these electrodes any gain from the fracture-induced lithium recovery is counterbalanced by the higher loss from the side reactions and CEI growth in contrast to the BL-rich and SL electrodes that manifest a decline of inactive lithium after 100 cycles (Fig. 3f).

The rate capability of the SL-poor and BL-poor electrodes is subjected to ceaseless deterioration on account of the monotonic rise in the fraction of disabled lithium (Fig. 3g). The evolution of the charge-transfer resistance is an indirect sign of particle fracture and variation in the active surface area of the NMC electrodes. The charge-transfer resistance decreases as long as the new interfaces remain electronically connected to the percolation network of the porous electrode. As such, the defective carbon wiring in the SL-poor and BL-poor electrodes is manifested in the sporadic increase of the charge transfer resistance (Fig. 3h and Table S2).

4. Conclusions

In this work, the synergistic interaction of the particle fracture and the electronic percolation network in the NMC622 electrodes was found momentous for the dynamics of aging in the LTO|NMC cells. The unusual observation of the energy recovery and the enhancement of the charge-transfer kinetics over extended cycling testified to a complex pattern for lithium (re)distribution in the cell triggered by the particle fracture. The fresh interfaces exposed to the electrolyte are vulnerable to the (electro)chemical side reactions but in parallel can facilitate the (de) insertion of lithium via a more kinetically favorable route of pore-wall flux in contrast to the solid-state diffusion. The net impact on the lithium inventory is influenced by the electrode microstructure and the configuration of its electronic percolation network. The fracture induced aging anomalies discussed in this paper highlight the need for considering the mechanical aspects in the optimization of the electrodes' formulation for high energy and durable lithium-ion battery electrodes.

Declaration of Competing Interest

The authors declare that they have no known competing financial interests or personal relationships that could have appeared to influence the work reported in this paper.

Acknowledgments

The authors are grateful for financial support to FWO-Vlaanderen (SBO XL-Lion, S005017N) and the Special Research Fund BOF of Hasselt University.

Appendix A. Supplementary data

Supplementary data to this article can be found online at https://doi.org/10.1016/j.elecom.2021.107134.

References

[1] A. Manthiram, An outlook on lithium ion battery technology, ACS Cent. Sci. 3 (2017) 1063–1069.

[2] J.U. Choi, N. Voronina, Y.-K. Sun, S.-T. Myung, Recent progress and perspective of advanced high-energy co-less Ni-rich cathodes for Li-ion batteries: yesterday, today, and tomorrow, Adv. Energy Mater. 10 (42) (2020) 2002027, https://doi.org/10.1002/aenm.v10.4210.1002/aenm.202002027.

[3] Y. Kuang, C. Chen, D. Kirsch, L. Hu, Thick electrode batteries: principles, opportunities, and challenges, Adv. Energy Mater. 9 (33) (2019) 1901457, https://doi.org/10.1002/aenm.v9.3310.1002/aenm.201901457.

[4] S. Müller, J. Eller, M. Ebner, C. Burns, J. Dahn, V. Wood, Quantifying inhomogeneity of lithium ion battery electrodes and its influence on electrochemical performance, J. Electrochem. Soc. 165 (2) (2018) A339–A344.

[5] H. Hamed, S. Yari, J. D'Haen, F.U. Renner, N. Reddy, A.n. Hardy, M. Safari, Demystifying charge transport limitations in the porous electrodes of lithium-ion batteries, Adv. Energy Mater. 10 (47) (2020) 2002492, https://doi.org/10.1002/aenm.v10.4710.1002/aenm.202002492.

[6] Y. Nomura, K. Yamamoto, T. Hirayama, E. Igaki, K. Saitoh, Visualization of lithium transfer resistance in secondary particle cathodes of bulk-type solid-state batteries, ACS Energy Lett. 5 (2020) 2098–2105.

[7] S. Lou, Q. Liu, F. Zhang, Q. Liu, Z. Yu, T. Mu, Y. Zhao, J. Borovilas, Y. Chen, M. Ge, X. Xiao, W.K. Lee, G. Yin, Y. Yang, X. Sun, J. Wang, Insights into interfacial effect and local lithium-ion transport in polycrystalline cathodes of solid-state batteries, Nat. Commun. 11 (2020) 5700.

[8] S. Yari, H. Hamed, J. D'Haen, M.K. Van Bael, F.U. Renner, A. Hardy, M. Safari, Constructive versus destructive heterogeneity in porous electrodes of lithium-ion batteries, ACS Appl. Energy Mater. 3 (2020) 11820–11829.

[9] M.K. Burdette-Trofimov, B.L. Armstrong, J. Nelson Weker, A.M. Rogers, G. Yang, E. C. Self, R.R. Armstrong, J. Nanda, G.M. Veith, Direct measure of electrode spatial heterogeneity: influence of processing conditions on anode architecture and performance, ACS Appl. Mater. Interfaces 12 (2020) 55954–55970.

[10] B.L. Trembacki, A.N. Mistry, D.R. Noble, M.E. Ferraro, P.P. Mukherjee, S. A. Roberts, Mesoscale analysis of conductive binder domain morphology in lithium-ion battery electrodes, J. Electrochem. Soc. 165 (2018) E725–E736.

[11] S. Vierrath, L. Zielke, R. Moroni, A. Mondon, D.R. Wheeler, R. Zengerle, S. Thiele, Morphology of nanoporous carbon-binder domains in Li-Ion batteries—a FIB-SEM study, Electrochem. Commun. 60 (2015) 176–179.

[12] N. Besnard, A. Etiemble, T. Douillard, O. Dubrunfaut, P. Tran-Van, L. Gautier, S. Franger, J.-C. Badot, E. Maire, B. Lestriez, Multiscale morphological and electrical characterization of charge transport limitations to the power performance of positive electrode blends for lithium-ion batteries, Adv. Energy Mater. 7 (8) (2017) 1602239, https://doi.org/10.1002/aenm.201602239.

[13] D.-W. Chung, P.R. Shearing, N.P. Brandon, S.J. Harris, R.E. García, Particle size polydispersity in Li-ion batteries, J. Electrochem. Soc. 161 (3) (2014) A422–A430.

[14] D. Kehrwald, P.R. Shearing, N.P. Brandon, P.K. Sinha, S.J. Harris, Local tortuosity inhomogeneities in a lithium battery composite electrode, J. Electrochem. Soc. 158 (12) (2011) A1393, https://doi.org/10.1149/2.079112jes.

[15] M. Ebner, D.-W. Chung, R.E. García, V. Wood, Tortuosity anisotropy in lithium-ion battery electrodes, Adv. Energy Mater. 4 (5) (2014) 1301278, https://doi.org/10.1002/aenm.201301278.

[16] D. Pritzl, A.E. Bumberger, M. Wetjen, J. Landesfeind, S. Solchenbach, H. A. Gasteiger, Identifying contact resistances in high-voltage cathodes by impedance spectroscopy, J. Electrochem. Soc. 166 (4) (2019) A582–A590.

[17] Z. Xu, M.M. Rahman, L. Mu, Y. Liu, F. Lin, Chemomechanical behaviors of layered cathode materials in alkali metal ion batteries, J. Mater. Chem. A 6 (2018) 21859–21884.

[18] X. Cheng, Y. Li, T. Cao, R. Wu, M. Wang, H. Liu, X. Liu, J. Lu, Y. Zhang, Real-time observation of chemomechanical breakdown in a layered nickel-rich oxide cathode realized by in situ scanning electron microscopy, ACS Energy Lett. 6 (2021) 1703–1710.

[19] A.O. Kondrakov, A. Schmidt, J. Xu, H. Geßwein, R. Mönig, P. Hartmann, H. Sommer, T. Brezesinski, J. Janek, Anisotropic lattice strain and mechanical degradation of high- and low-nickel NCM cathode materials for Li-ion batteries, J. Phys. Chem. C 121 (2017) 3286–3294.

[20] R. Xu, H. Sun, L.S. de Vasconcelos, K. Zhao, Mechanical and structural degradation of $LiNi_xMn_yCo_zO_2$ cathode in Li-ion batteries: an experimental study, J. Electrochem. Soc. 164 (13) (2017) A3333–A3341.

[21] G. Sun, T. Sui, B. Song, H. Zheng, L. Lu, A.M. Korsunsky, On the fragmentation of active material secondary particles in lithium ion battery cathodes induced by charge cycling, Extreme Mech. Lett. 9 (2016) 449–458.

[22] S. Bessette, A. Paolella, C. Kim, W. Zhu, P. Hovington, R. Gauvin, K. Zaghib, Nanoscale lithium quantification in $Li_XNi_yCo_wMn_ZO_2$ as cathode for rechargeable batteries, Sci. Rep. 8 (2018) 17575.

[23] J. Nanda, J. Remillard, A. O'Neill, D. Bernardi, T. Ro, K.E. Nietering, J.-Y. Go, T. J. Miller, Local state-of-charge mapping of lithium-ion battery electrodes, Adv. Funct. Mater. 21 (2011) 3282–3290.

[24] Y. Yang, R. Xu, K. Zhang, S.-J. Lee, L. Mu, P. Liu, C.K. Waters, S. Spence, Z. Xu, C. Wei, D.J. Kautz, Q. Yuan, Y. Dong, Y.-S. Yu, X. Xiao, H.-K. Lee, P. Pianetta, P. Cloetens, J.-S. Lee, K. Zhao, F. Lin, Y. Liu, Quantification of heterogeneous degradation in Li-ion batteries, Adv. Energy Mater. 9 (25) (2019) 1900674, https://doi.org/10.1002/aenm.v9.2510.1002/aenm.201900674.

[25] H. Zhou, K. An, S. Allu, S. Pannala, J. Li, H.Z. Bilheux, S.K. Martha, J. Nanda, Probing multiscale transport and inhomogeneity in a lithium-ion pouch cell using in situ neutron methods, ACS Energy Lett. 1 (2016) 981–986.

[26] N. Shpigel, M.D. Levi, X. Cheng, T. Cao, R. Wu, T.S. Mathis, Y. Zhang, D. Aurbach, Y. Gogotsi, Diffusion-induced transient stresses in Li-battery electrodes imaged by electrochemical quartz crystal microbalance with dissipation monitoring and environmental scanning electron microscopy, ACS Energy Lett. 4 (8) (2019) 1907–1917.

[27] C.D. Quilty, D.C. Bock, S. Yan, K.J. Takeuchi, E.S. Takeuchi, A.C. Marschilok, Probing sources of capacity fade in $LiNi_{0.6}Mn_{0.2}Co_{0.2}O_2$ (NMC622): an operando XRD study of Li/NMC622 batteries during extended cycling, J. Phys. Chem. C 124 (2020) 8119–8128.

[28] Y. Ruan, X. Song, Y. Fu, C. Song, V. Battaglia, Structural evolution and capacity degradation mechanism of $LiNi_{0.6}Mn_{0.2}Co_{0.2}O_2$ cathode materials, J. Power Sources 400 (2018) 539–548.

[29] C. Tian, F. Lin, M.M. Doeff, Electrochemical characteristics of layered transition metal oxide cathode materials for lithium ion batteries: surface, bulk behavior, and thermal properties, Acc. Chem. Res. 51 (1) (2018) 89–96.

[30] N.Y. Kim, T. Yim, J.H. Song, J.-S. Yu, Z. Lee, Microstructural study on degradation mechanism of layered $LiNi_{0.6}Co_{0.2}Mn_{0.2}O_2$ cathode materials by analytical transmission electron microscopy, J. Power Sources 307 (2016) 641–648.

[31] E. Trevisanello, R. Ruess, G. Conforto, F.H. Richter, J. Janek, Adv. Energy Mater. 11 (2021) 2003400.

[32] M. Safari, C. Delacourt, Aging of a Commercial Graphite/$LiFePO_4$ Cell, J. Electrochem. Soc. 158 (10) (2011) A1123, https://doi.org/10.1149/1.3614529.

[33] R. Ruess, S. Schweidler, H. Hemmelmann, G. Conforto, A. Bielefeld, D.A. Weber, J. Sann, M.T. Elm, J. Janek, Influence of NCM particle cracking on kinetics of lithium-ion batteries with liquid or solid electrolyte, J. Electrochem. Soc. 167 (10) (2020) 100532, https://doi.org/10.1149/1945-7111/ab9a2c.